Optimal voxel size for measuring global gray and white matter proton metabolite concentrations using chemical shift imaging

[1,2]LARS G. HANSON, [1]ELFAR ADALSTEINSSON, [3]ADOLF PFEFFERBAUM, [1]DANIEL M. SPIELMAN

[1]Dept. of Diagnostic Radiology, Stanford University, Stanford, CA, USA

[2]Danish Research Center for Magnetic Resonance and

Dept. of Chemistry, University of Copenhagen, Denmark

[3] SRI International, Menlo Park, CA, USA

Accepted: *Magnetic Resonance in Medicine*, Feb. 22, 2000

Running head: Optimal voxel size for gray and white matter spectroscopy

Correspondence to:

Lars G. Hanson

Danish Research Center for Magnetic Resonance

Hvidovre Hospital, afs. 340

Kettegård Allé 30

DK-2650 Hvidovre

Denmark

Phone: +45 36 32 29 76

Fax: +45 36 47 03 02

email: larsh@magnet.drcmr.dk

Abstract

Quantification of gray and white matter levels of spectroscopically visible metabolites can provide important insights into brain development and pathological conditions. Chemical shift imaging offers a gain in efficiency for estimation of global gray and white matter metabolite concentrations compared to single voxel methods. In the presented study, the optimal voxel size is calculated from segmented human brain data and accompanying field maps. The optimal voxel size is found to be approximately 8 cc, but a wide range of values, 4 cc-64 cc, can be chosen with little increase in estimated concentration error ($< 15\ \%$).

Key words: spectroscopic imaging; gray and white matter spectroscopy; optimal voxel size

1 INTRODUCTION

Many normal and pathological conditions are reflected in metabolite concentrations in the brain. Some changes are known or suspected to be present globally in gray or white matter. They are associated with normal development (1–3) as well as pathology, e.g. AIDS related dementia, Alzheimers disease and schizophrenia, (4–8). Quantification of spectroscopically visible metabolites, measured in brain gray matter (GM) and white matter (WM) separately, can provide important insights into brain development and pathological conditions.

Chemical shift imaging (CSI) normally offer less precise localization than single voxel spectroscopy (SVS), but it provides increased efficiency due to the extended spatial coverage (9), thus making CSI the method of choice for global gray and white matter spectroscopy.

Care is needed in the calculation of separate GM and WM spectra from CSI data since many voxels will contain a mixture of tissues as well as cerebral spinal fluid (CSF). Knowledge of the spatial distribution of tissues is required for calculating separate spectra for individual tissue types. Linear regression can be used to estimate the variation of metabolite concentrations with voxel tissue composition (2, 3, 10–12) thus providing a means of accounting for partial volume effects. Acquisition of high-resolution data with subsequent spatial averaging suffers a signal-to-noise ratio (SNR) loss compared to low-resolution imaging with the same effective voxel size. Consequently, the choice of voxel size involves a trade-off of SNR in individual voxels versus tissue composition variation and insensitivity to shim and subcutaneous lipids that tend to contaminate spectra.

The present study addresses this trade-off and aims at finding the optimal voxel size. The regression method provides a good starting point as it takes full advantage of all available data and provides concentration error estimates.

The paper is organized as follows: A theoretical framework for the calculation of concentration variances is established, and their general properties are derived analytically. Field maps and segmentation data from *in vivo* studies of normal subjects are used to cal-

culate the relative accuracies of concentration estimates as a function of voxel size.

2 METHODS

Given spectroscopic and segmented brain data for a range of spatial resolutions, metabolite concentrations in each compartment and their variances can be estimated along with the optimal voxel size. This approach is not feasible for the present study, mainly because it requires very lengthy measurements. An analytic approach based on the regression method provides a better way as relative accuracies of gray and white matter metabolite concentrations can be determined using only field maps, segmented structural images and *a priori* knowledge of metabolite properties.

Section 2.1 concerns combining data from all locations, while sections 2.2 and 2.3 describe the individual effects responsible for the voxel size dependence of the concentration accuracy. Section 2.4 concerns the analysis of signals from individual voxels and section 2.5 describes how the method was applied to *in vivo* data.

2.1 VARIANCE OF GM AND WM CONCENTRATION ESTIMATES

For a given metabolite, linear regression can be used to estimate the concentration $y = a + bx$ versus GM fraction x ($0 \leq x \leq 1$) based on observations (x_i, y_i) for each voxel labeled by index $i = 1 \ldots N$, Fig. 1. The constants a and b provide pure white and gray matter metabolite concentration estimates, $y_{\text{WM}} = y(x = 0) = a$ and $y_{\text{GM}} = y(x = 1) = a + b$, given by the two endpoints of the graph (2, 10, 11). The presence of CSF does not pose further difficulty under normal conditions, as metabolite concentrations in this substance are known to be exceedingly small. For a given metabolite, the local concentration in brain is proportional to the ratio of MR-visible metabolite protons, c_i, to brain volume, B_i, i.e. $y_i = kc_i/B_i$. The segmentation is assumed to be precise compared to the spectroscopic measurements so that no uncertainty is associated with the x_i's or the B_i's.

The best estimates $\hat{a}, \hat{b}$ of a and b can be calculated using well-known formulas (13)

when noise is normally distributed with zero mean and variance $\sigma_i^2 \equiv \sigma^2(y_i)$. The variances of $\hat{a}$ and $\hat{b}$ are of more interest in the present context as well as the variance, σ_{GM}^2 corresponding to the endpoint $y(x = 1)$:

$$\text{White matter:} \qquad \sigma_{\text{WM}}^2 \equiv \sigma_a^2 = \Delta^{-1} \sum x_i^2/\sigma_i^2 \qquad [1]$$

$$\text{Gray matter:} \qquad \sigma_{\text{GM}}^2 = \Delta^{-1} \sum (1 - x_i)^2/\sigma_i^2 \qquad [2]$$

$$\text{Regression slope:} \qquad \sigma_b^2 = \Delta^{-1} \sum 1/\sigma_i^2 \qquad [3]$$

$$\text{with} \qquad \Delta \equiv \sum 1/\sigma_i^2 \sum x_i^2/\sigma_i^2 - \left(\sum x_i/\sigma_i^2 \right)^2 . \qquad [4]$$

The summations are over all voxels labeled by index i. Our aim is to minimize σ_{WM}^2, σ_{GM}^2 and σ_b^2 with respect to voxel size. Normally, the concentration difference is of interest, and reliable measures of both end-points ($x = 0, 1$) are wanted, Fig. 1. This is ensured if the slope $b = y_{\text{GM}} - y_{\text{WM}}$ is well determined. Minimizing σ_b is a natural choice that will be adapted in the following.

The uncertainties in metabolite concentration

$$\sigma_i = \sigma(y_i) = k\sigma(c_i)/B_i \equiv r_i \sigma_0 / B_i \qquad [5]$$

are factorized, thus defining a common uncertainty σ_0 for all voxels and a voxel specific scaling, r_i. All common noise terms, such as sequence and acquisition specific parameters, determine σ_0. The concentration error estimate also depends on the metabolite line shape and hence on the local shim. This dependence is expressed in the quantity r_i being a measure of the sensitivity of the peak area estimate to noise. The influence of inhomogeneity is described qualitatively and quantitatively in sections 2.3 and 2.4, respectively.

Weighting factors $W_i = \sigma_0^2/\sigma_i^2$ as well as normalized weights, $\tilde{W}_i = W_i/W$ where $W = \sum W_i$, are introduced to simplify Eq. [3]. The slope uncertainty is expressed in terms of a weighted variance $\text{Var}_{\tilde{W}_i}(x_i)$ being large when the GM fraction differs much between voxels as seen in Fig. 1.

$$\sigma_b^2 = \frac{\sigma_0^2/W}{\text{Var}_{\tilde{W}_i}(x_i)} \qquad \text{with} \qquad [6]$$

$$\text{Var}_{\tilde{W}_i}(x_i) \equiv \sum x_i^2 \tilde{W}_i - \left(\sum x_i \tilde{W}_i \right)^2 \qquad [7]$$

Interpretations of these equations are given in sections 2.2 and 2.3. The calculation of the error estimates $\sigma(c_i)$ are the subject of section 2.4.

2.2 PARTIAL VOLUME EFFECTS

Imaging of a particular volume of interest with small voxels gives rise to an increased number of voxels with effectively only one type of tissue (uncontaminated voxels). Pure gray and white matter spectra are only badly determined from large voxels if these all have similar tissue composition, Fig. 1. On the other hand, it does not help to decrease the voxel size much below the minimum dimension of the structures of interest, since this will not increase the fraction of uncontaminated voxels further. The advantage of small voxels with respect to partial voluming, is reflected in the appearance of the GM fraction variance in the denominator that decreases as a function of voxel size, Eq. [6].

2.3 SHIM AND DIRECT VOLUME EFFECTS

The numerator in Eq. [6] also has a strong voxel size dependence. The general dependence is inaccessible for now, as a calculation requires specific knowledge of the factors $\sigma(c_i)$. Qualitative insight can nevertheless be gained by examining the limits of homogeneous and inhomogeneous broadening, e.g. when linewidths are independent of voxel size ($T2^* \simeq$ T2), and when linewidths are dominated by inhomogeneities ($T2^* \ll$ T2). The two limits correspond to small and large voxels relative to the typical length scale of macroscopic field inhomogeneities (the phase coherence length that depends on the evolution period). T2 is never exactly equal to $T2^*$ even for very small voxels since inhomogeneities exist on a microscopic length scale. The T2-values are used as an approximation to the largest possible $T2^*$ that differ from T2 by less than 10%.

Direct volume effect When line shapes are dominated by irreversible T2-processes,

$$W \propto \sum B_i^2 = \frac{V^2}{N}\left(\frac{1}{N}\sum f_i^2\right) \equiv (V^2/N)F(N). \qquad [8]$$

N is defined as the number of voxels and V is the total examined volume. The brain matter voxel fraction f_i is given by $f_i = B_i N/V$. This rewriting makes the dominant N dependence explicit, as the mean-square of the voxel fraction, $F(N) \equiv \frac{1}{N}\sum f_i^2$, is generally a slowly varying function compared to $1/N$. In the limit of homogeneous broadening, the following approximate relationship can be established:

$$\sigma_b^2 \propto \frac{N}{\mathrm{Var}_{\tilde{W}_i}(x_i)} \qquad [9]$$

The denominator is independent of N in the limit of small voxels, i.e., when voxels fit easily within all anatomical structures, and the direct volume effect therefore causes σ_b^2 to be inversely proportional to the voxel volume.

B_0 field inhomogeneity Errors due to field differences between voxels, i.e. intervoxel inhomogeneity, can be corrected with the help of a water reference (14, 15) while intravoxel inhomogeneity causes broadening of spectral peaks. Three effects are of relevance: More noise is introduced into area estimation of broad peaks, peak overlap reduces the precision in peak area estimation, and baseline variations are difficult to distinguish from broad peaks.

It is useful to consider the limit of inhomogeneous broadening for estimating shim effects. For the shims and voxel sizes of interest, the residual B_0-field gradient is well approximated as linear across any voxel while direction and magnitude will differ from voxel to voxel. The voxel volume is V/N and the spread of B_0 field magnitudes is therefore proportional to $(V/N)^{1/3}$ for cubic voxels. Area estimation is essentially integration of the spectral signal density over the width of the peak that is determined by the local shim. Noise is evenly distributed over frequency, and the variance $\sigma^2(c_i)$ (and hence r_i^2) consequently scales as $(V/N)^{1/3}$ in the limit of inhomogeneous broadening.

$$\mathrm{Var}(c_i) \propto (\mathrm{T2}_i^*)^{-1} \propto N^{-1/3} \qquad [10]$$

This relation implies that inhomogeneities approximately cause the slope variance to be proportional to the linear voxel dimension, disregarding all other effects than broadening. Similar to the case of homogeneous broadening, the sum of weights W is now

expressed as $W = (V^2/N)N^{1/3}F'(N)$ defining the slowly varying function $F'(N) \equiv \frac{1}{N}\sum f_i^2 / \left(N^{1/3} r_i^2\right)$. It follows that in this limit

$$\sigma_b^2 \propto \frac{N^{2/3}}{\mathrm{Var}_{\tilde{W}_i}(x_i)} \qquad [11]$$

2.4 SPECTRAL DECOMPOSITION

Sections 2.2 and 2.3 provide insight into the trade-offs involved in choosing a voxel size. Proceeding further requires a discussion of peak area quantification for voxelwise estimation of the uncertainties in metabolite content, $\sigma(c_i)$, appearing in Eq. [5]. These depend on the intrinsic lineshape and shim as will be shown.

The metabolites are generally well-characterized in terms of resonance frequencies, coupling constants and approximate relaxation properties. Lineshapes can therefore be calculated voxelwise for each of the metabolites with the help of a water reference scan. An expansion of the measured signal $\mathbf{S}$ (or a projection, $\tilde{\mathbf{S}}$, of it) onto the basis of non-orthogonal, metabolite basis vectors, provides proton density estimates for each metabolite.

A design matrix $\mathbf{A}$ is formed with columns given by the normalized basis vectors. Linear estimation of the metabolite concentrations amounts to determining coefficients, $\mathbf{a}$, so that $\tilde{\mathbf{S}} = \mathbf{A}\mathbf{a}$ (16). Fast and reliable numeric singular value decomposition (SVD) implementations exist, providing matrices $\mathbf{U}$, $\mathbf{T}$ and $\mathbf{V}$ so that $\mathbf{A} = \mathbf{U}\mathbf{T}\mathbf{V}^T$, where $\mathbf{U}$ and $\mathbf{V}$ are orthogonal, $\mathbf{T}$ is a diagonal matrix of singular values, T_{mm}, and $\mathbf{V}^T$ is $\mathbf{V}$ transposed (13). These matrices can be used to calculate a pseudo-inverse of $\mathbf{A}$ that multiplied onto $\mathbf{S}$ (or $\tilde{\mathbf{S}}$) provides the coefficients $\mathbf{a}$. The variances express the separability of the metabolite signals, and are given by

$$\sigma^2(a_j) = \sum_m \left(\frac{V_{jm}}{T_{mm}}\right)^2. \qquad [12]$$

The coefficients are measures of the energies in the various metabolite signals. The metabolite concentrations at the echo time are proportional to the areas under the projections provided all spin-spin-interactions are refocused.

$$\sigma^2(c_j) = \left(\sum_m A_{mj}\right)^2 \sigma^2(a_j) \qquad [13]$$

The specific baseline distortions are not known *a priori*, but can be modeled as superpositions of a few additional well-chosen basis functions, (17, 18).

Figure 2 shows an example basis calculated from a modeled water reference signal. It is chosen to include the metabolite signals, baseline distortions and unsuppressed water and lipid signals. The basis is designed for echo planar spectroscopy (19), where the spectral bandwidth is typically rather limited since it is traded off for spatial resolution and/or gradient strength (e.g. 300 Hz $\simeq$ 4.6 ppm at 1.5 Tesla). This detail is reflected as aliasing of water in the constructed basis, but the methods and results are of a general nature. The following metabolites are included: N-acetyl-compounds (NAc, approximated by a singlet at 2.0 ppm, T2 $\simeq$ 450 ms), choline (Cho, singlet at 3.2 ppm, T2 $\simeq$ 360 ms), creatine/phosphocreatine (Cr, singlet at 3.0 ppm, T2 $\simeq$ 210 ms), lactate (Lac, doublet at 1.3 ppm separated by 6.94 Hz (20), T2 $\simeq$ 450 ms). The transverse relaxation times are given for $B_0 = 1.5$ T (21). Only the primary MR-visible spectral structures are included. Basis vectors are constructed from the water free induction decay (FID) by proper frequency shifting and T2-correction.

Further spectral structure results from unsuppressed water (T2$\simeq$ 100 ms for brain water, T2$\simeq$1 s for CSF (22)). The line shape can not easily be characterized because it depends on the B_0-inhomogeneity, the radio-frequency field amplitude and the longitudinal relaxation time T1. The remaining water signal typically has spectral width and approximate center frequency similar to the unsuppressed water signal. It is well modeled by a superposition of water reference spectra shifted slightly in frequency taking into account the aliasing associated with the low spectral bandwidth of echo planar spectroscopy.

SVD provides the most probable linear decomposition of measured spectra into separate metabolite signals as well as error estimates. The concentration errors are independent of the signal, and depend linearly on the spectral noise density σ_0. The variations with voxel and molecule are determined by the specifics of the metabolite basis functions; their widths and degree of orthogonality in particular.

2.5 ACQUISITION AND ANALYSIS OF HUMAN BRAIN DATA

Fifteen normal human subjects were studied using a 1.5 Tesla GE Signa MR-scanner equipped with the standard head coil in order to calculate the actual dependence of the regression error on voxel-size. The method is briefly outlined before details are discussed: For each of the subjects studied, high resolution anatomical images were acquired and used for classification of the brain tissues (segmentation). B_0 field maps were measured after shimming and were subsequently resliced to fit anatomical slices. Calculations were performed for each value in a range of spatial resolutions relevant for spectroscopic imaging:

1. High resolution field maps and segmented brain data were down-sampled using rectangular or sinc-shaped voxels.

2. The following calculations were done for each low-resolution voxel: A water reference was modeled from the intravoxel field distribution. This was used along with *a priori* knowledge of metabolite and baseline properties for constructing a basis for the linear analysis. The variances of the individual metabolite coefficients were calculated.

3. Tissue composition variances and estimated concentration errors were used for a calculation of the regression slope error.

Variances for all spatial resolutions were finally compared to determine the optimum voxel size.

Anatomical images of 16 oblique and consecutive 3.2 mm slices covering approximately the top third of the brain were acquired with sub-millimeter in-plane resolution (matrix 256^2, field of view $(24\text{ cm})^2$). A semi-automatic segmentation procedure was used to classify each voxel as either GM, WM, CSF or other, and the images were subsequently down-sampled to matrix 128^2 to limit calculation time and memory requirements. Details of the acquisition and segmentation can be found in (3). Three dimensional B_0 field maps were acquired after volume selective higher-order shimming of the same region (23). These were resliced to match the segmented data.

The tissue and field distributions for a range of larger voxel-sizes were calculated from the high-resolution data. The severity of partial volume problems are determined mainly by the largest voxel dimension for imaging of isotropic regions. A rather large section of the brain was examined for the present study, and there are no obvious directions in which long rectangular voxels can be advantageously aligned. Consequently, cubic voxels are near optimal with respect to partial volume effects for a given voxel volume, and only such voxels were considered.

Spatial down-sampling Sinc- and rectangular spatial point spread functions (PSFs) were compared since deviations from rectangular voxels are far-reaching for low resolution imaging. Fourier imaging with rectangular k-space coverage results in a sinc-shaped PSF. The shape in the slice selection direction was taken to be rectangular in both cases, since slice profiles can generally be made quite good in multi-slice studies using pulse shaping (24).

The GM distribution in the voxels of a low-resolution study with sinc PSF was found by truncating the "true" k-space density that is well approximated by the Fourier transformed high-resolution GM image. For rectangular voxels the similar data reduction was performed by adding high-resolution tissue densities within low-resolution voxels in real space.

Because of the finite k-space sampling density of the segmented images, exact equal voxel dimensions can not be obtained without time consuming regridding. To avoid this, each voxel dimension was chosen as a multiple of the slice thickness, and the in-plane dimension was subsequently chosen as close as possible to ensure near-cubical voxels. The deviations from cubic shape results in less than 7 percent difference between maximum and minimum dimensions for sinc-shaped voxels and less than 15 percent for rectangular voxels.

Water reference modeling The construction of the metabolite sub-basis was done using a water reference calculated voxelwise from the B_0 field map and structural data, taking

into account the PSF. This approach excludes effects from line shape distortions not due to inhomogeneity (e.g. eddy currents). The B_0 field distribution within each voxel was obtained by discretizing the measured field maps in 32 steps and representing the field as 32 spectral-spatial density maps that were down-sampled separately. The non-equidistant steps of discretization were chosen so that every bin corresponded to equal amounts of brain. This was done on the basis of a histogram of B_0 values to minimize round-off errors. High resolution masks were computed for each B_0 interval. These field density maps were reduced to low resolution using the methods described above, and the field distribution was used to model water FIDs.

Calculation of variances Once the water references, corresponding basis functions, and factors $\sigma(c_i)$ were calculated using SVD, Eq. [6] was used to calculate the variance of the slope σ_b^2. The dependence on voxel size was established by repeating the calculation.

3 RESULTS

The figures 2-5 show properties of representative data acquired for a healthy male volunteer, age 31 years. The segmented data and the B_0 field maps shown in Fig. 3, provide the necessary data for determining the optimal voxel size. The corresponding B_0-histogram illustrating the shim quality in Fig. 4 was used to minimize total round-off errors when discretizing the field maps. Figure 5 show example images before and after down-sampling using the described algorithm. Similar matrix size reductions were performed for the individual field density maps. The intravoxel shims are illustrated for the two PSFs under consideration in Fig. 6 for all of the 15 normal subjects.

An example basis calculated from a modeled water reference is shown in Fig. 2. The metabolite separabilities calculated voxelwise and the tissue composition variances, Fig. 7, enters the calculation of the concentration variances. The relative importance of voxel size for shim, tissue distribution and direct volume effects affecting the concentration variances, are illustrated in Fig. 8. These are the factors influencing the accuracy of the regression

shown in Fig. 9 for a range of voxel sizes. The figures show the means for the 15 subjects as well as the ranges of variation. A shallow minimum in the variance is found for cubic voxels with approximately 2 cm edge.

The shapes of the curves shown in Fig. 9 changed insignificantly when calculations were carried out for different metabolites and when the gray and white matter concentration variances were calculated rather than the regression slope error.

4 DISCUSSION

The tissue composition variance shown in Fig. 7, reflects the overall structure of the imaged volume and the partial volume problems increasing with voxel size. The curves are relatively smooth due to the lack of distinct typical dimensions in the brain. For smaller voxels yet, the curves will converge to particular values, but the data do not support reliable curves for resolutions exceeding the slice thickness 3.2 mm.

The intravoxel field inhomogeneity increases with voxel size as illustrated in Fig. 6. The global shim is reflected in the local shim for sinc-shaped voxels due to the sinc side lobes.

The trade-off between intravoxel field homogeneity, partial volume, and direct voxel size effects is illustrated in Fig. 8. These effects are responsible for the existence of an optimal voxel size that can can be estimated from Fig. 9 showing the variance of the NAc concentration estimate. The variance is found to be remarkably insensitive to voxel volume changing less than a factor of 5 over 3-4 orders of magnitude. A shallow minimum in the concentration variance is found for 8 cc voxels for sinc PSF, leading us to conclude that the advantage of resolving gray matter structures is outweighed by the resulting SNR penalty, Fig. 9.

Only for voxels smaller than 4 cc is there a pronounced loss of accuracy. Even this, however, is somewhat compensated by the fact that imaging with the smallest voxels reduces demands on lipid suppression (25). The relative significance of this depends on the method of lipid suppression under consideration. Typical methods are volume pre-selection by

STEAM or PRESS (26, 27), outer volume suppression (OVS, (28)), or T1-selective inversion recovery (29). Approximately 30% gain in SNR, can be obtained by imaging without lipid suppression, compared to measurements with T1-selective suppression by inversion recovery. This potential gain is not included in the calculation. Similar losses result from OVS that often suppresses or distorts signals from cortex, therefore mainly affecting gray matter and potentially creating artificial systematic GM/WM signal differences.

Sinc shaped voxels resulting from unweighted Fourier reconstruction were compared to rectangular voxels to determine the influence of voxel shape. Hadamard encoding (30), filtering or weighted acquisition (31) are techniques affecting the voxel shape. Sinc shaped and rectangular voxels represents two extremes, and interestingly, little effect is found between the two, as long as the exact voxel shape is taken into consideration.

As a consequence, the choice of voxel size is fairly free when focus is on global gray and white matter metabolite concentrations. Often, however, sub-structures are of interest (such as individual hemispheres), and the results suggest that the voxels can be chosen optimally for such structures without sacrificing much overall accuracy. An immediate consequence is that there is little difference between optimizing for gray matter, white matter or both simultaneously, as was done here. Similarly, a reduction of the available brain volume by spatial pre-selection or OVS can change the optimal voxel size slightly.

A simple strategy for gray/white matter segmentation was chosen. Potential misclassification of pixels at tissue boundaries will not cause a significant difference considering the insensitivity of the presented results to anatomical details (minor intersubject variation).

For simplicity, the brain water T2s were assumed equal for gray and white matter thus neglecting the approximate 10% difference. The linewidths are determined by the inhomogeneity also, and the GM/WM linewidth difference is no more than 5% even for the smallest voxels used. The change in linewidth over the range of voxel-size under consideration, is much larger, and the GM/WM T2 difference will therefore not influence the result significantly. The brain T2 value was used as an approximation to $T2^*$ in the limit of small voxels. This causes an underestimation of the concentration error estimate for the smallest

voxels (<5%).

Very little intersubject variation is found after correction for individual differences in brain matter volume. The irregular functional dependence seen in Fig. 9 is not random noise, but rather manifestations of brain structure and shim.

An uninteresting source of structure is the voxel shape that is only approximately cubic (within 15%). Small changes in volume associated with changes in shape, appear at 30, 40 and 50 mm linear dimension being approximated by the third root of the volume. Resulting changes of slope are particularly visible in the graphs illustrating shim quality, Fig. 6.

Linear estimation provides a flexible and reliable tool for quantifying metabolite concentrations and confidence intervals even when baseline distortions are present. A basis was constructed to model everything but random noise (metabolites, baseline distortions, residual water and lipids). Whereas the individual coefficients depend much on the choice of basis, this is not the case for the metabolite concentration estimates. Broad Lorentzians were used to model the unknown baseline. Other authors have used splines or polynomials (17, 18). The difference is marginal, as any basis spanning the subspace of slowly varying functions provide similar results.

The required computer memory and calculation time was reduced by discretizing the B_0 field. The round-off error was minimized by adapting the steps of the discretization to the measured B_0 field. Calculations with increasing numbers of bins were performed, suggesting that the number of bins used was sufficient to ensure convergence.

The results depend on the quality of the shim since $T2^*$ is voxel size dependent. We used data acquired after volume selective higher-order shimming (23). Often higher-order shim coils are not present, adjusted for best global performance, or not used at all because of the extra time required for adjustment. The optimal voxel size is reduced correspondingly if CSI is performed with worse shims than used here.

The regression approach can be extended to handle more complicated problems such as determining metabolite concentrations in GM/WM for the hemispheres separately. Multidimensional linear least squares fitting readily handles extra classes of tissue. Subdivision

of brain structures is expected to decrease the optimal voxel size.

When water references and *a priori* knowledge is available, the problem can be linearized as was done here. The extremely bad SNRs ($\ll 1$) experienced for the smallest voxels are not problematic even though metabolite estimates will be equally noisy – weighted averaging will still produce the best estimates, given that the spectral model is correct. The problem can no longer be linearized if non-additive quantities like chemical shifts need to be estimated on a voxel by voxel basis. In that case, good SNR in all voxels is crucial. Non-linear and non-parametric methods should be avoided when possible and large voxels should be used whenever such methods are needed. The linearity of the problem also results in the optimal voxel size being independent of the performance of the CSI method and of the metabolite concentrations. The variance of the parameters estimated by regression scales with the noise variance of the samples, while the relative errors for various voxel sizes do not change.

5 Conclusion

Aspects of the choice of voxel size for global gray and white matter spectroscopy were discussed in detail and qualitative results for the accuracy of concentration estimates were given. The actual dependence on voxel size was determined for *in vivo* studies of normal volunteers. This was found to be a remarkably weak function of the voxel size with a shallow minimum for 8 cc voxels. Less than 15% variation occurs for voxel-sizes ranging from 4 cc to 64 cc. The voxel shape has little influence on the accuracy as long as the correct shape is used for the calculations. The presented methods can readily be extended to determine optimal acquisition parameters when specific regions beyond global gray and white matter are of special interest.

REFERENCES

1. E. B. CADY, J. PENRICE, P. N. AMESS, A. LOREK, M. WYLEZINSKA, R. F. ALDRIDGE, F. FRANCONI, J. S. WYATT, AND E. O. REYNOLDS, Lactate, N-acetylaspartate, choline and creatine concentrations, and spin-spin relaxation in thalamic and occipito-parietal regions of developing human brain. *Magn Reson Med* **36**, 878-86 (1996).

2. K. O. LIM AND D. M. SPIELMAN, Estimating NAA in cortical gray matter with applications for measuring changes due to aging. *Magn Reson Med* **37**, 372-7 (1997).

3. A. PFEFFERBAUM, E. ADALSTEINSSON, D. SPIELMAN, E. V. SULLIVAN, AND K. O. LIM, *In vivo* spectroscopic quantification of the N-acetyl moiety, creatine, and choline from large volumes of brain gray and white matter: Effects of normal aging. *Magn Reson Med* **41**, 276-84 (1999).

4. P. B. BARKER, R. R. LEE, AND J. C. MCARTHUR, AIDS dementia complex: Evaluation with proton MR spectroscopic imaging. *Radiology* **195**, 58-64 (1995).

5. C. D. MARCUS, S. D. TAYLOR-ROBINSON, J. SARGENTONI, J. G. AINSWORTH, G. FRIZE, P. J. EASTERBROOK, S. SHAUNAK, AND D. J. BRYANT, ^{1}H MR spectroscopy of the brain in HIV-1-seropositive subjects: Evidence for diffuse metabolic abnormalities. *Metab Brain Dis* **13**, 123-36 (1998).

6. P. F. KWO-ON-YUEN, R. D. NEWMARK, T. F. BUDINGER, J. A. KAYE, M. J. BALL, AND W. J. JAGUST, Brain N-acetyl-L-aspartic acid in Alzheimer's disease: A proton magnetic resonance spectroscopy study. *Brain Res* **667**, 167-74 (1994).

7. K. O. LIM, E. ADALSTEINSSON, D. SPIELMAN, E. V. SULLIVAN, M. J. ROSENBLOOM, AND A. PFEFFERBAUM, Proton magnetic resonance spectroscopic imaging of cortical gray and white matter in schizophrenia. *Arch Gen Psychiatry* **55**, 346-52 (1998).

8. A. PFEFFERBAUM, E. ADALSTEINSSON, D. SPIELMAN, E. V. SULLIVAN, AND K. O. LIM, *In vivo* brain concentrations of N-acetyl compounds, creatine, and choline in Alzheimer disease. *Arch Gen Psychiatry* **56**, 185-92 (1999).

9. A. MACOVSKI, Noise in MRI. *Magn Reson Med* **36**, 494-7 (1996).

10. T. J. DOYLE, B. J. BEDELL, AND P. A. NARAYANA, Relative concentrations of proton MR visible neurochemicals in gray and white matter in human brain. *Magn Reson Med* **33**, 755-9 (1995).

11. H. P. HETHERINGTON, J. W. PAN, G. F. MASON, D. ADAMS, M. J. VAUGHN, D. B. TWIEG, AND G. M. POHOST, Quantitative ^{1}H spectroscopic imaging of human brain at 4.1 T using image segmentation. *Magn Reson Med* **36**, 21-9 (1996).

12. G. F. MASON, W. J. CHU, J. T. VAUGHAN, S. L. PONDER, D. B. TWIEG, D. ADAMS, AND H. P. HETHERINGTON, Evaluation of 31P metabolite differences in human cerebral gray and white matter. *Magn Reson Med* **39**, 346-53 (1998).

13. W. PRESS, S. TEUKOLSKY, W. VETTERLING, AND B. FLANNERY, "Numerical Recipes in C (The Art of Scientific Computing)". Cambridge University Press, 1992.

14. D. SPIELMAN, P. WEBB, AND A. MACOVSKI, Water referencing for spectroscopic imaging. *Magn Reson Med* **12**, 38-49 (1989).

15. U. KLOSE, *In vivo* proton spectroscopy in presence of eddy currents. *Magn Reson Med* **14**, 26-30 (1990).

16. D. M. SPIELMAN, P. WEBB, AND A. MACOVSKI, A statistical framework for *in vivo* spectroscopic imaging. *J Magn Reson* **79**, 66-77 (1988).

17. S. W. PROVENCHER, Estimation of metabolite concentrations from localized *in vivo* proton NMR spectra. *Magn Reson Med* **30**, 672-9 (1993).

18. R. LAATIKAINEN, M. NIEMITZ, W. J. MALAISSE, M. BIESEMANS, AND R. WILLEM, A computational strategy for the deconvolution of NMR spectra with multiplet structures and constraints: Analysis of overlapping 13C-2H multiplets of 13C enriched metabolites from cell suspensions incubated in deuterated media. *Magn Reson Med* **36**, 359-65 (1996).

19. P. MANSFIELD, Spatial mapping of the chemical shift in NMR. *Magn Reson Med* **1**, 370-86 (1984).

20. P. B. KINGSLEY, Scalar coupling and zero-quantum coherence relaxation in STEAM: Implications for spectral editing of lactate. *Magn Reson Med* **31**, 315-9 (1994).

21. B. J. SOHER, P. C. VAN ZIJL, J. H. DUYN, AND P. B. BARKER, Quantitative proton MR spectroscopic imaging of the human brain. *Magn Reson Med* **35**, 356-63 (1996).

22. P. A. BOTTOMLEY, T. H. FOSTER, R. E. ARGERSINGER, AND L. M. PFEIFER, A review of normal tissue hydrogen NMR relaxation times and relaxation mechanisms from 1-100 MHz: Dependence on tissue type, NMR frequency, temperature, species, excision, and age. *Med Phys* **11**, 425-48 (1984).

23. D. M. SPIELMAN, E. ADALSTEINSSON, AND K. O. LIM, Quantitative assessment of improved homogeneity using higher-order shims for spectroscopic imaging of the brain. *Magn Reson Med* **40**, 376-82 (1998).

24. J. PAULY, P. LE ROUX, AND D. NISHIMURA, Parameter relations for the Shinnar-Le Roux selective excitation pulse design algorithm. *IEEE Trans Med Imaging* **10**, 53-65 (1991).

25. L. G. HANSON AND O. B. PAULSON, Segmented Spectroscopy: A flexible alternative to single voxel methods, *in* "Proc. of the ISMRM 6^{th} Annual Meeting", p. 363, 1998.

26. J. FRAHM, H. BRUHN, M. L. GYNGELL, K. D. MERBOLDT, W. HANICKE, AND R. SAUTER, Localized high-resolution proton NMR spectroscopy using stimulated echoes: Initial applications to human brain *in vivo*. *Magn Reson Med* **9**, 79-93 (1989).

27. P. A. BOTTOMLEY, Spatial localization in NMR spectroscopy *in vivo*. *Ann NY Acad Sci* **508**, 333-48 (1987).

28. J. H. DUYN, J. GILLEN, G. SOBERING, P. C. VAN ZIJL, AND C. T. MOONEN, Multisection proton MR spectroscopic imaging of the brain. *Radiology* **188**, 277-82 (1993).

29. D. M. SPIELMAN, J. M. PAULY, A. MACOVSKI, G. H. GLOVER, AND D. R. ENZMANN, Lipid-suppressed single- and multisection proton spectroscopic imaging of the human brain. *J Magn Reson Imaging* **2**, 253-62 (1992).

30. L. BOLINGER AND J. S. LEIGH, Hadamard spectroscopic imaging (HSI) for multivolume localization. *J Magn Reson* **80**, 162-167 (1988).

31. D. L. PARKER, G. T. GULLBERG, AND P. R. FREDERICK, Gibbs artifact removal in magnetic resonance imaging. *Med Phys* **14**, 640-5 (1987).

Figure Captions

Figure 1: The trade-off between voxel-size and SNR. The regression method aims at determining the concentrations $y(x = 0)$ and $y(x = 1)$ corresponding to pure white and gray matter respectively. The estimate is based on observations (x_i, y_i) for each voxel. If not for noise, all observations would be on a straight line provided the tissues are homogeneous. If voxels are large, few points are acquired with a relatively good SNR. More and noisier data with a larger spread of x_i-values are provided when the voxel size is decreased. The total noise increases when the voxel size is reduced with fixed total volume and acquisition time.

Figure 2: Basis used for calculation of r_i for a typical small voxel. Non-Lorentzian lines result from inhomogeneous broadening. The frequency shift reflects that water is not at resonance in this voxel. Water is aliased since the calculation is made to match echo planar spectroscopy, where bandwidths are rather limited. The results are of a general nature, though.

Figure 3: Segmented high-resolution data (a) and corresponding field maps (b). The segmentation data are color-coded as follows: WM is colored white, GM is light gray, CSF is dark gray and black is used for all other specimens including background. The shim is generally very good with major inhomogeneities spatially restricted to the region above the air-filled sinuses. The actual field values and the quality of the shim can be estimated by comparison to the B_0-histogram shown in Fig. 4.

Figure 4: Histogram of B_0 values in the entire imaged region reflecting the overall quality of the shim in the ROI. The field is given relative to the carrier which is adjusted to the water resonance. The discretization of B_0 values was done so that the area under this curve was near equal in all 32 B_0 intervals.

Figure 5: Example down-sampled gray matter distributions used for the calculations. The upper left image shows the gray matter in the top slice of the high-resolution dataset. The

following eight images illustrate the corresponding down-sampled images for resolutions used in the calculation. The PSF is sinc-like and voxels are approximately cubic, so the slice thickness differs between images. The framed image corresponds to the calculated optimal resolution (see Fig. 9).

Figure 6: Intravoxel inhomogeneity for each of the 15 subjects averaged over voxels. (a) The 15 curves show the B_0 standard deviation for sinc-PSF and (b) the corresponding curves for rectangular voxels. Inhomogeneities within voxels decrease with voxel size, but differences are apparent for the two voxel shapes: The shim of small rectangular voxels is relatively independent of the global shim compared to that of sinc-shaped voxels with the same nominal linear dimension. This is due to the sinc side lobes and is reflected in the curves converging for small rectangular voxels. There is a stronger dependence on voxel size for rectangular voxels for the same reason. The wide intersubject spread shows that the global shim quality varies considerably, but effects of inhomogeneity are reduced for small voxels.

Figure 7: The tissue composition variance $\mathrm{Var}(x_i)$ as a function of voxel dimension for sinc-shaped (solid line) and rectangular (dashed line) voxels. These are approximately cubic with the linear voxel dimension calculated as the third root of the volume. The purity of voxels with respect to tissue composition is reflected in the variance that increases as the voxel volume is decreased. Rectangular voxels are better localized than sinc-shaped voxels with the same volume. This advantage shows for voxels smaller than the anatomical structures, where sidelobes contribute much partial tissue volume.

Figure 8: Illustration of the variation with voxel dimension of the three factors influencing the NAc concentration accuracy for one subject and sinc PSF: voxel purity, voxel volume and shim. The solid line is the inverse of the tissue purity in voxels, $\mathrm{Var}(x_i)^{-1/2}$, which enters as a factor in the calculation of σ_b, Eq. [6]. The dotted curve depicts $N^{1/2}$ and illustrates the direct influence of voxel volume on the estimate. The dashed curve is $(\sum_i \mathrm{Var}(c_i)\tilde{W}_i)^{1/2}$ and is therefore a measure of the importance of shim. The graphs are

scaled individually to have unit maximum. The three effects are combined in the calculation of σ_b, Fig. 9 – shim and voxel purity are favored by small voxels, but a strong voxel size dependence push for large voxels.

Figure 9: The variation of σ_b for NAc with voxel dimension for approximately cubic, sinc-shaped (solid line) and rectangular (dashed line) voxels. The error bars indicate the mean absolute deviations for the 15 normal subjects – very limited variation is found. Imaging with rectangular voxels is seen to give better results for the smallest voxels due to the shim advantage and minimal partial volume effect. The variation of σ_b is remarkably slow except for the smallest voxels, considering that the ratio of maximal to minimal voxel volume is 4400 for this range of voxel dimensions. Less than 15% variation is found for voxel-sizes ranging from 4 cc to 64 cc. The optimal voxel dimension minimizing σ_b is seen to be approximately 2 cm for sinc-PSF, corresponding to the middle right image in Fig. 5.

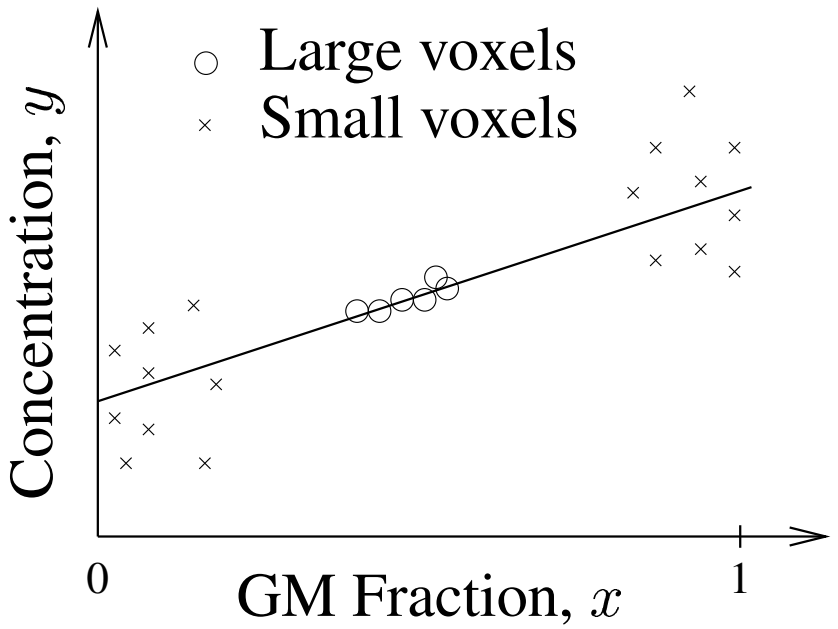

Figure 1:
The trade-off between voxel-size and SNR. The regression method aims at determining the concentrations $y(x = 0)$ and $y(x = 1)$ corresponding to pure white and gray matter respectively. The estimate is based on observations (x_i, y_i) for each voxel. If not for noise, all observations would be on a straight line provided the tissues are homogeneous. If voxels are large, few points are acquired with a relatively good SNR. More and noisier data with a larger spread of x_i-values are provided when the voxel size is decreased. The total noise increases when the voxel size is reduced with fixed total volume and acquisition time.

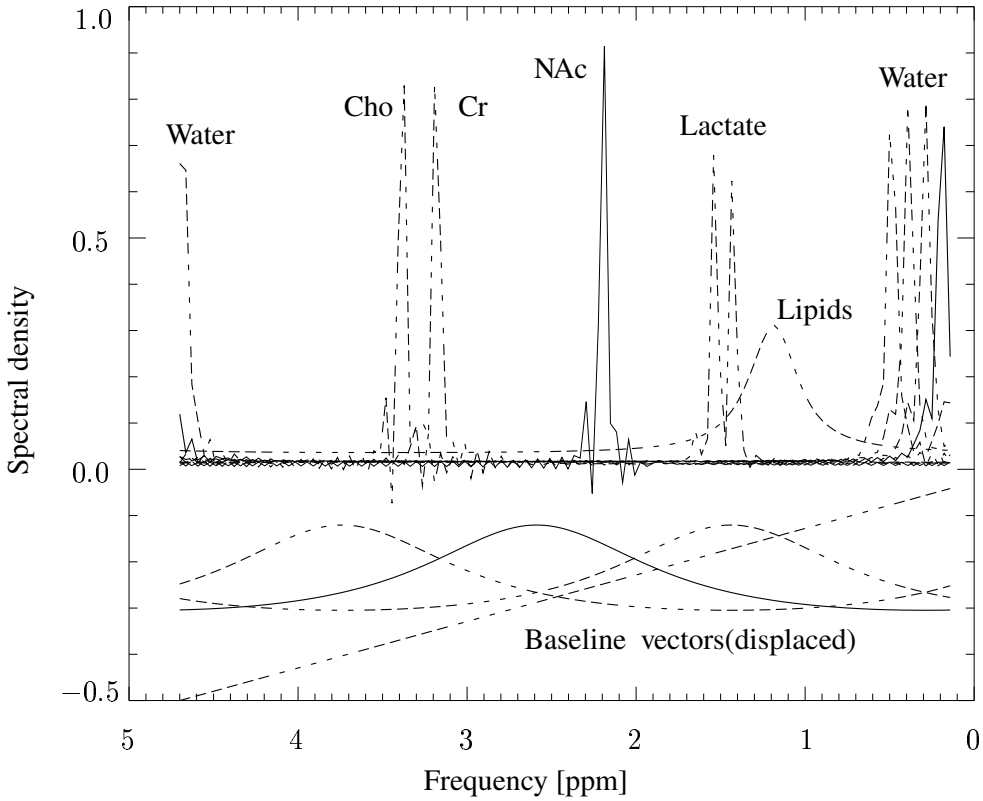

Figure 2:
Basis used for calculation of r_i for a typical small voxel. Non-Lorentzian lines result from inhomogeneous broadening. The frequency shift reflects that water is not at resonance in this voxel. Water is aliased since the calculation is made to match echo planar spectroscopy, where bandwidths are rather limited. The results are of a general nature, though.

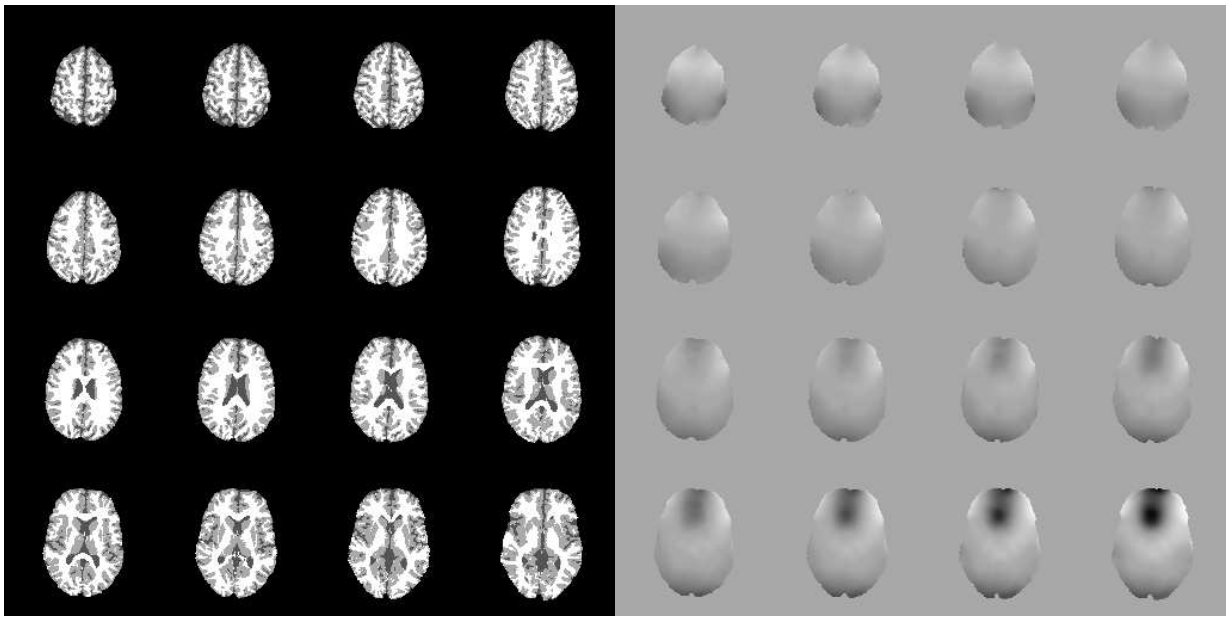

(a) (b)

Figure 3:
Segmented high-resolution data (a) and corresponding field maps (b). The segmentation data are color-coded as follows: WM is colored white, GM is light gray, CSF is dark gray and black is used for all other specimens including background. The shim is generally very good with major inhomogeneities spatially restricted to the region above the air-filled sinuses. The actual field values and the quality of the shim can be estimated by comparison to the B_0-histogram shown in Fig. 4.

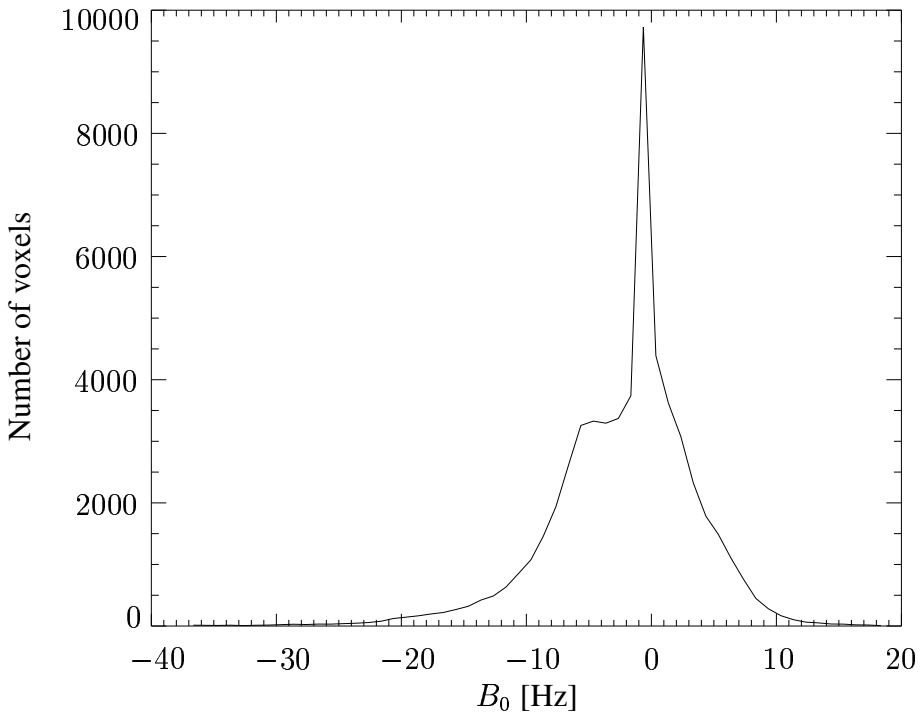

Figure 4:
Histogram of B_0 values in the entire imaged region reflecting the overall quality of the shim in the ROI. The field is given relative to the carrier which is adjusted to the water resonance. The discretization of B_0 values was done so that the area under this curve was near equal in all 32 B_0 intervals.

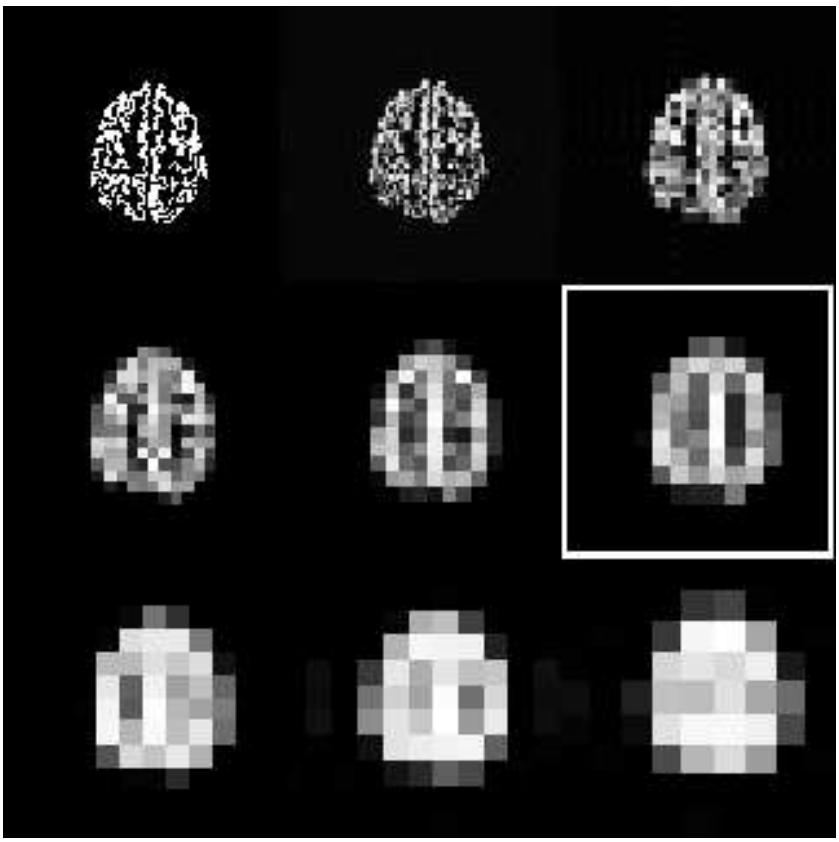

Figure 5:
Example down-sampled gray matter distributions used for the calculations. The upper left image shows the gray matter in the top slice of the high-resolution dataset. The following eight images illustrate the corresponding down-sampled images for resolutions used in the calculation. The PSF is sinc-like and voxels are approximately cubic, so the slice thickness differs between images. The framed image corresponds to the calculated optimal resolution (see Fig. 9).

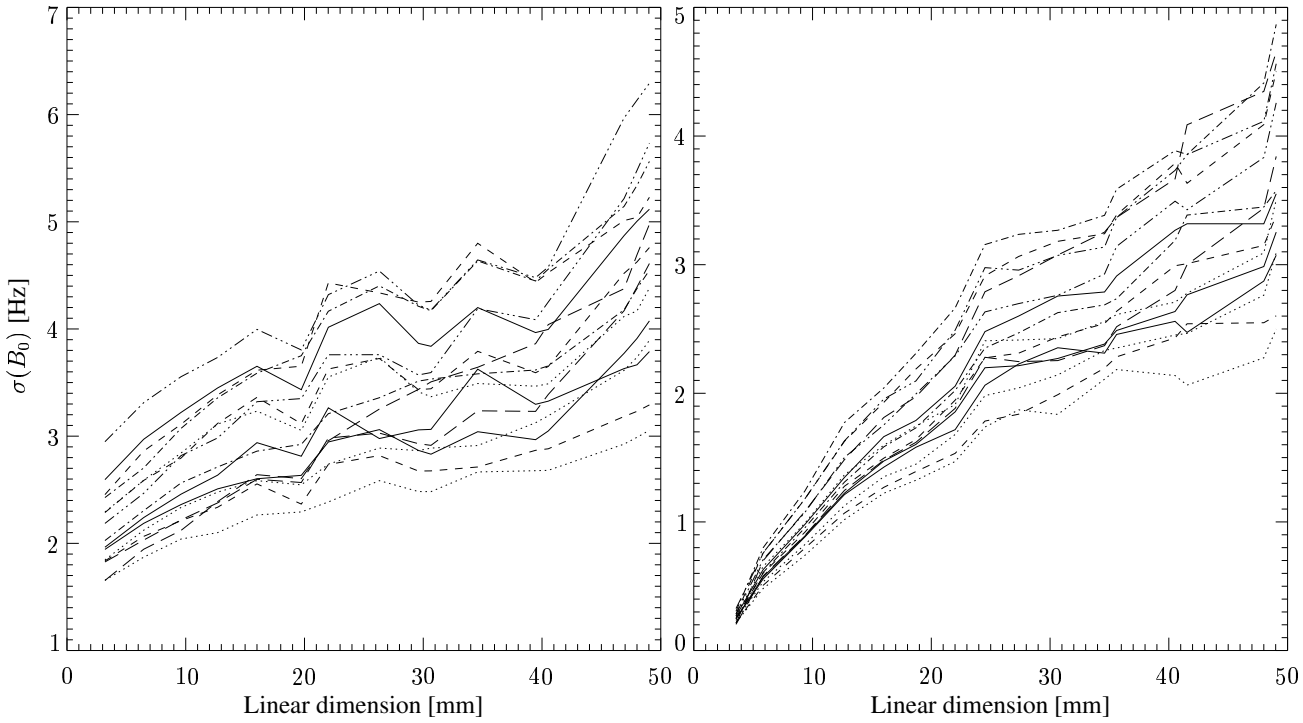

(a) (b)

Figure 6:

Intravoxel inhomogeneity for each of the 15 subjects averaged over voxels. (a) The 15 curves show the B_0 standard deviation for sinc-PSF and (b) the corresponding curves for rectangular voxels. Inhomogeneities within voxels decrease with voxel size, but differences are apparent for the two voxel shapes: The shim of small rectangular voxels is relatively independent of the global shim compared to that of sinc-shaped voxels with the same nominal linear dimension. This is due to the sinc side lobes and is reflected in the curves converging for small rectangular voxels. There is a stronger dependence on voxel size for rectangular voxels for the same reason. The wide intersubject spread shows that the global shim quality varies considerably, but effects of inhomogeneity are reduced for small voxels.

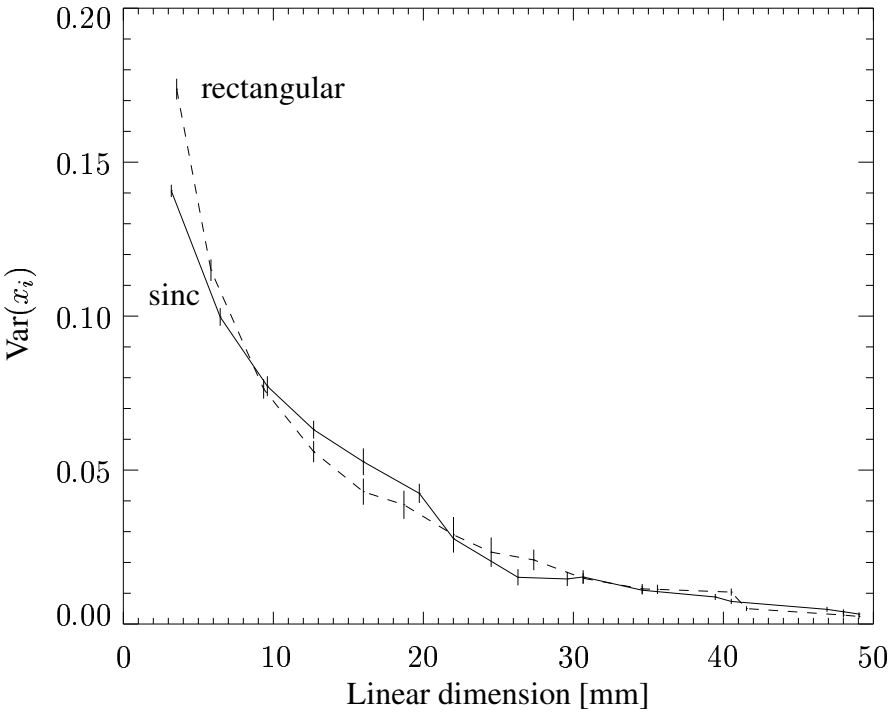

Figure 7:
The tissue composition variance Var(x_i) as a function of voxel dimension for sinc-shaped (solid line) and rectangular (dashed line) voxels. These are approximately cubic with the linear voxel dimension calculated as the third root of the volume. The purity of voxels with respect to tissue composition is reflected in the variance that increases as the voxel volume is decreased. Rectangular voxels are better localized than sinc-shaped voxels with the same volume. This advantage shows for voxels smaller than the anatomical structures, where sidelobes contribute much partial tissue volume.

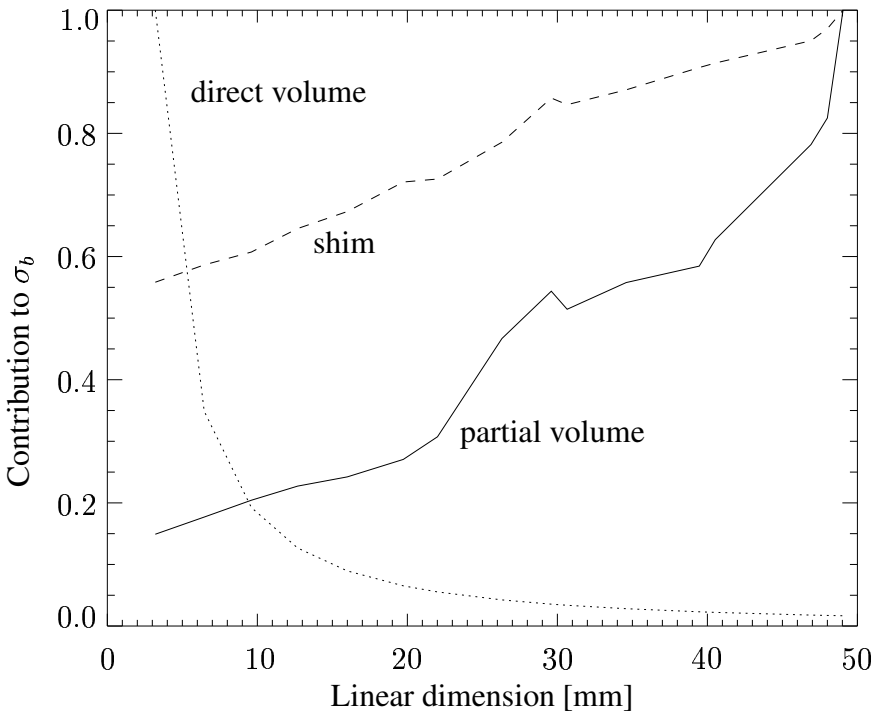

Figure 8:
Illustration of the variation with voxel dimension of the three factors influencing the NAc concentration accuracy for one subject and sinc PSF: voxel purity, voxel volume and shim. The solid line is the inverse of the tissue purity in voxels, $\mathrm{Var}(x_i)^{-1/2}$, which enters as a factor in the calculation of σ_b, Eq. [6]. The dotted curve depicts $N^{1/2}$ and illustrates the direct influence of voxel volume on the estimate. The dashed curve is $(\sum_i \mathrm{Var}(c_i)\tilde{W}_i)^{1/2}$ and is therefore a measure of the importance of shim. The graphs are scaled individually to have unit maximum. The three effects are combined in the calculation of σ_b, Fig. 9 – shim and voxel purity are favored by small voxels, but a strong voxel size dependence push for large voxels.

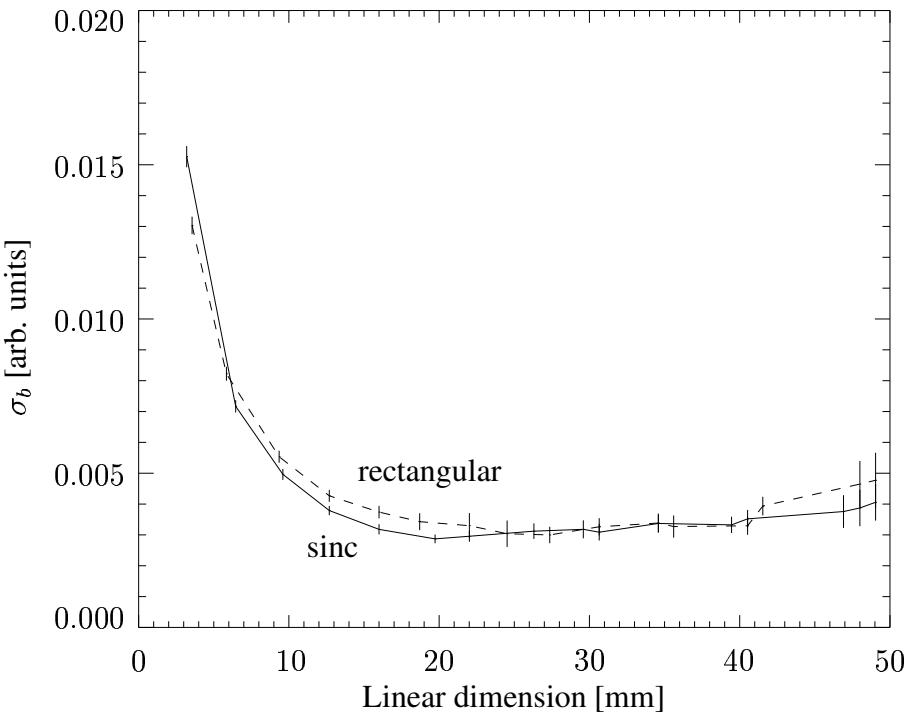

Figure 9:
The variation of σ_b for NAc with voxel dimension for approximately cubic, sinc-shaped (solid line) and rectangular (dashed line) voxels. The error bars indicate the mean absolute deviations for the 15 normal subjects – very limited variation is found. Imaging with rectangular voxels is seen to give better results for the smallest voxels due to the shim advantage and minimal partial volume effect. The variation of σ_b is remarkably slow except for the smallest voxels, considering that the ratio of maximal to minimal voxel volume is 4400 for this range of voxel dimensions. Less than 15% variation is found for voxel-sizes ranging from 4 cc to 64 cc. The optimal voxel dimension minimizing σ_b is seen to be approximately 2 cm for sinc-PSF, corresponding to the middle right image in Fig. 5.